*minerals*

MDPI

*Article*

# Robust Estimation and Validation of Contact Parameters of Iron Ore for Transfer Chute Simulation

**Guilherme Pereira de Oliveira [1,2], Rodrigo Magalhães de Carvalho [1,*], Henrique Peixoto de Souza Almeida [1] and Luís Marcelo Tavares [1]**

[1] Department of Metallurgical and Materials Engineering, Universidade Federal do Rio de Janeiro, Rio de Janeiro 21941-972, Brazil; guilherme.oliveira@coppe.ufrj.br or guilherme.pereira.oliveira@vale.com (G.P.d.O.); henrique@metalmat.ufrj.br (H.P.d.S.A.); tavares@metalmat.ufrj.br (L.M.T.)
[2] Vale S.A., Port of Tubarão, Vitória 29090-860, Brazil
* Correspondence: rodrigo@metalmat.ufrj.br; Tel.: +55-21-981197394

**Abstract:** Transfer chutes are crucial components in handling bulk materials using belt conveyors. The flow of material through these devices is influenced by several variables. Traditionally, these devices have been designed based on prior experience. However, the increase in computational capacity has enabled the application of the Discrete Element Method (DEM) in their simulation by modeling the behavior of individual particles forming the bulk. The greatest challenge in this process is the selection of appropriate contact models and parameters that accurately reflect the material response. The work describes an approach used to calibrate contact parameters of a sample of moist iron ore while interacting with two distinct surface materials. The methodology starts with a variety of bench-scale tests, followed by experiments in a pilot-scale handling system, concluding with a semi-quantitative verification in an industrial-scale chute using three commercial DEM software. The findings indicate that certain tests are more responsive to specific material behavior, so that their combined use allows for a realistic representation of the material flow, even when using virtual spherical particles.

**Keywords:** discrete element method; transfer chute; iron ore; bulk materials handling; parameter calibration

check for updates

Academic Editor: Manoj Khanal

Received: 8 January 2025
Revised: 7 February 2025
Accepted: 12 February 2025
Published: 14 February 2025

**Citation:** de Oliveira, G.P.; de Carvalho, R.M.; de Souza Almeida, H.P.; Tavares, L.M. Robust Estimation and Validation of Contact Parameters of Iron Ore for Transfer Chute Simulation. *Minerals* **2025**, *15*, 175. https://doi.org/10.3390/min15020175

**Copyright:** © 2025 by the authors. Licensee MDPI, Basel, Switzerland. This article is an open access article distributed under the terms and conditions of the Creative Commons Attribution (CC BY) license (https://creativecommons.org/licenses/by/4.0/).

## 1. Introduction

### 1.1. Overview

Belt conveyors are the most widely used devices for the continuous transportation of ores in the minerals industry, with applications that span from mines and processing plants across entire logistic chain up to the client's site. For instance, the largest mining company in Brazil has over 1800 belt conveyors in its production facilities, and about 400 conveyors with a total length of 180 km in its logistics terminals. Transfer chutes play a key role in systems that rely on conveyor belts since they allow for the material flow to be re-directed to either other directions or other devices. Since each conveyor has at least one transfer chute, thousands of chutes are used in the mining chain in this company alone.

Failures in transfer chutes can impact the entire production chain, causing losses due to the unavailability of the asset. Reestablishing operation after clogging is an arduous and time-consuming task. Large chutes may take several hours to be purged after blocking, exposing personnel to inherent but avoidable risks. In addition, legislation and society are becoming increasingly less tolerant to fugitive material such as those generated in transfer chutes. Furthermore, frequent stops—scheduled or not—to replace worn and torn

components reduce equipment availability. Such issues demonstrate the importance and the challenges at the project stage of correctly sizing transfer chutes for systems handling bulk solids.

A number of variables related to the design of a chute, including its maximum throughput, the drop height, the distance between transfer points, the feeding and receiving belt velocities, and the chute slope angle, directly affect its performance [1]. These, coupled with the characteristics of the bulk material being handled, namely, its composition, size distribution, particle shape, bulk density, and moisture content, make each transfer chute operation virtually unique. Relatively modest changes in those variables may result in the appearance of problems such as clogging, excessive wear of structural components, belt misalignment, spillage, and dust emissions [1,2].

Over the years, several concepts have been proposed regarding chute design [3], many of which rely on prior experience [1–4], and these have had their share of successes and failures in guiding the design of new chutes. Fortunately, the increase in computational processing capacity and the new solvers that became available in recent years provide very good conditions for the use of the Discrete Element Method (DEM) [5]. Developed in the 1970s, this technique has evolved to become the workhorse in the analysis and simulation of ore flow in industrial-scale transfer chutes [6–12].

DEM reproduces the collective granular material behavior obtained through solving Newton's second law of motion for each individual particle element in the system, which makes it ideally suited for the simulation of handling operations involving ore particles, since they are naturally discretized systems. However, it is not computationally feasible to predict the response of all particles that are present in a real ore handling system, since it may contain particles with sizes that range from micrometers to several decimeters. Furthermore, reproducing real particles is challenging, since each particle is unique in terms of shape [13]. Therefore, in order to perform DEM simulations at the pace that is required for industrial application, several simplifications must be made to the simulated system. Fortunately, it has been shown that the bulk behavior of irregularly-shaped fine particles may be reproduced using a technique called coarse graining [14]. This consists of keeping some key quantities constant at the particle scale or simply using particles that are coarser and that have a simpler geometry but are still able to represent the behavior of the system [14]. The aim of these simplifications is to reproduce the behavior of fine and irregularly-shaped particles with coarse and less complex particles in the simulations [15,16]. This coarse graining approach has been used successfully, for instance, to simulate material flow in silos [17], dense medium cyclones [18], rotating drums [19] and ore grabbers [20]. The selection of the appropriate contact model and appropriate contact parameters to model particle–particle and particle–surface collisions is an integral part of this approach.

The parameter calibration required for dry non-cohesive materials is well-documented and covered by several authors, with good summaries presented by Coetzee [21,22]. It is considered consensus that DEM can replicate the flow of non-cohesive granular materials with good accuracy. However, when cohesive materials are considered, the mechanism becomes significantly more complex [23–25]. Several authors proposed different approaches for DEM contact parameter calibration, from direct measurements [26] to optimization algorithms that are compared to experimental data [21,24,27,28].

On the other hand, in spite of the great importance of understanding the flow of cohesive materials, particularly moist iron ore fines, there is still only a limited number of papers dealing with this topic, especially when focused on large-scale industrial simulations. For instance, simulation studies dealing with iron ore fines can be found in the field of agglomeration [29]. In addition, the grab operation of cohesive iron ores from Carajás was modeled considering a 50% passing size of 0.88 mm [30], presenting a four-step

DEM calibration procedure for the cohesive material. The authors concluded that the coefficients of static friction, surface energy parameters, and particle shear modulus were the most significant continuous variables for the simulated processes. Recently, Scheffler and Coetzee [14] reviewed the calibration procedures for cohesive bulk materials and stated that the parameter calibration of such types of materials requires more research.

There is a growing demand for simulations of bulk solids flows at the industrial scale through the application of DEM. Recently, a chute arrangement transferring coal (free flowing material) in a real high-throughput installation was successfully simulated, with predictions being compared to site observations [31]; in addition, a sampling with cross-stream cutters in a gold mining company was simulated to investigate the practicality of the rules and recommendations established as principles for the correct extraction of samples in industrial sampling devices [32]. DEM was used in a pelleting process to improve the performance of a dryer chute that discharges sticky iron ore fines, showing poor flowability [33]. An industrial chute handling iron ore with a high moisture content was simulated to investigate the influence of four different liners in the material flowrate [34]. The loading of bulk materials in ships was modeled to determine the optimal use of space in the hold [35] and the stability of iron ore bulk cargoes during marine transport was modeled at a real-life scale to set measures to prevent instabilities resulting from cargo slip [36].

A critical issue in DEM simulation is testing for parameter calibration. Although a large number of tests have been proposed, from laboratory to pilot scale, including tests that provide direct measurements of a given parameter, no single test or set of tests are yet recognized as standard for calibration of the models [37,38]. In addition, when one calibrates the parameters against experimental data, there is usually not a unique set of parameters that can represent the data within the accepted experimental error [38]. Among these combinations of parameters that may be able to represent the tests with good accuracy, it is desired to identify the one that best represents the industrial system of interest. This means that additional experiments or measurements may be used to reduce the degrees of freedom in parameter optimization [15]. Additionally, the relative importance of these tests in identifying the optimal sets of parameters should be balanced against their sensitivity to certain contact parameters [37,38].

Therefore, a robust parameter calibration strategy that incorporates several aspects of the granular flow of moist iron ore fines is needed. The calibration must be robust in the sense that the material's behavior is reproduced with high fidelity in bench-scale experiments as well as in industrial-scale operations while ensuring the feasibility of running large-scale simulations.

### *1.2. Contact Models and Particle Model Selection in DEM*

The use of the Discrete Element Method to represent granular flow requires the choice of appropriate contact models. Usually, the contact force models are decoupled in one direction, which is either normal or tangential. The DEM codes generally use a linear spring and dashpot model in both the normal and the tangential direction, with an additional frictional slider in the tangential direction [39]. Owing to its simplicity, this form of model has been able to describe, with good accuracy, the bulk behavior of particles passing through handling operations [12,40]. Additionally, regarding the contact model, Weerasekara et al. [39] state that the idealized nature of the contact model does not allow for a detailed analysis of the contact events, so one should not over-interpret the individual contact events in terms of their physical significance, but the contact outputs can be used in particle degradation models since the energy dissipation is captured in the dashpot.

The most widely used models include the Hertz Model [41] for the normal direction and the Mindlin and Deresiewicz Model [42] for the tangential direction. The combination of both is popularly known as the Hertz–Mindlin Contact Model, which is currently implemented in leading DEM software [39].

In the Discrete Element Method, interactions are not restricted to collisions and contacts resulting in repulsion between particles and boundaries. A particle positioned close to another particle or a boundary can also interact through adhesive or cohesive forces. Per this definition, cohesion is the molecular force between similar particles that acts to unite them, while adhesion is the attraction force between differing molecules [43,44]. Although cohesion and adhesion have similar meanings, in solids bulk flow it is preferable to use the term "cohesion" for interactions between particles and "adhesion" for interactions between a particle and a boundary in the medium [43]. Both are attractive forces that explain a very common phenomenon in the flow of iron ore, where part of the material adheres to vertical walls of transfer chutes, even opposing the force of gravity. In finer and drier materials, the main adhesive forces are related to Van der Waals bonds and electrostatic forces. In wet materials, liquid bridges between particles are often the most important sources of adhesive forces. These liquid bridges are formed by the capillary condensation of low-viscosity fluid in the small contact zones between particles. Due to the surface tension of the liquid, the particles appear to be attracted to each other [45].

The correct modeling of forces is essential to represent the flow of sticky ores, which typically have a high moisture content. To represent the effects of cohesion/adhesion forces, elastic–adhesive contact models were developed, with the best known being the Johnson–Kendell–Roberts (JKR) model for normal elastic–adhesive contact [46]. The authors [46] extended the Hertz model to two elastic adhesive spheres using an energy balance approach. Alternatively, open-language-based software often uses a simplified version of the JKR Model to represent the adhesive contact, which is a modified form of the JKR Model proposed by Johnson et al. [46], identified as SJKR [47]. With this model, if two particles are in contact, an additional normal force is added that attempts to maintain the contact, which is proportional to the contact area of the particles and the density of the cohesion energy, given in $J/m^2$ [48]. Other modeling approaches can be used to model the cohesive behavior of bulk materials. For instance, Huynh et al. [49] have assessed the ability of Easo Liquid-Bridge (ELB) [50] to reproduce drawdown experiments and observed that it took less time to reach a stable state than the SJKR model. Ajmal et al. [47] performed a comparative calibration of the SJKR model and the full JKR, together with an adhesive hysteretic rolling resistance model, using a standard drawdown experiment.

Besides the selection of contact model and corresponding parameters, the modeling of the particle in a virtual environment also requires the selection of the particles' shape and size. At present, almost all DEM software has the ability to deal with different particle shapes, such as super quadrics, sphere clusters, or polyhedral shapes. However, the use of non-spherical particles results in higher computational effort being required to perform the simulations [51]. Spherical particles make contact detection easier through a comparison the spatial location of the sphere, considering its radius. In this case, the orientation of the particle is indifferent. This simple reduction in the degree of freedom substantially diminishes the computational cost [52].

Alternatively, any particle, no matter how complex its shape, can be represented by superimposing spheres. However, this involves greater computational cost depending on the desired level of complexity [52]. Virtual particle shapes that are very close to reality are more accurate, but they are also computationally expensive or even unfeasible for use in large-scale simulations [51,52]. As such, the selected particle shape must always represent a balance between the desired fidelity and the available computational capacity. Whether

using complex representations that nearly match the real particle shape or simply spheres, the most important criterion in the selection of the optimal particle shape to be used is its ability to computationally represent the real behavior of the material [26,37,53].

One technique that has been adopted when individual spheres are used to represent the response of complex real particle shapes is to increase the rolling friction coefficient to mimic the geometric difficulty of rolling of an irregularly shaped particle. This contrasts with the ease at which spherical particles roll under the action of tangential forces [25,54]. Rolling resistance is the name given to the momentum that opposes the rolling motion of a particle, which is very useful to describe the response of non-spherical particles when using spherical virtual particles. The two main rolling resistance models found in DEM software are classified as "Type A" and "Type C" [54,55]. The models classified as "Type A" apply a constant torque to the particle, whereas in the Type C models the torque consists of two components: a mechanical spring torque and a viscous damper.

The aim of this work is to present a robust multi-scale parameter calibration methodology for DEM simulations of large-scale operations handling iron ore fines in the presence of moisture using the available contact models in three of the most widely used commercial DEM simulation software. The procedure started with bench (small)-scale experiments, followed by their reproduction in a DEM environment, with varying values of contact parameters being used until the sets that best reproduced the behavior of the ore were obtained. Afterwards, handling experiments were carried out at the pilot (meso) scale, and their results were used in the final selection and verification of the material and contact model parameters. Finally, large-scale simulations were performed, and their results were compared with operation and maintenance records from an industrial transfer chute.

## 2. Methodology

### *2.1. Overview*

Figure 1 summarizes the calibration methodology, based on four stages: materials selection; experiments with a gradual increase in scale, starting with bench-scale experiments, before moving to pilot-scale, and finally using industrial scale as the full-scale verification.

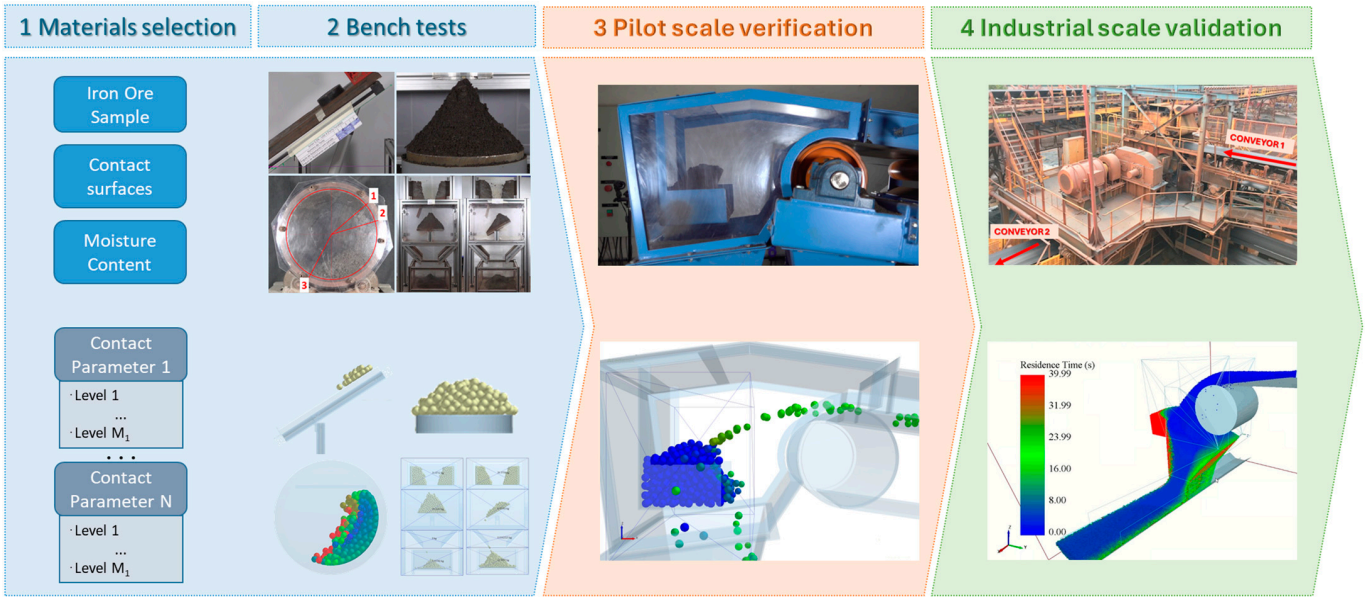



**Figure 1.** Summary of the calibration methodology based on an increase in scale, from bench tests to industrial-scale validation.

### *2.2. Materials*

The tests were conducted with a sinter feed sample with 6.5% moisture content (wet basis). The bulk density of the sinter feed sample was obtained by filling a container subject to vibration and measuring the mass and level of the material inside the container. The size distribution of the particles was measured using a combination of sieving and laser diffraction: 80% passing 2.88 mm and 20% passing size 0.40 mm, with a top size of 12.5 mm. The chemical composition of the sample was analyzed using an energy-dispersive X-ray fluorescence spectrometer, Simutix 14 (Rigaku, Tokyo, Japan), and is reported in Table 1. The ore was mainly composed of hematite and quartz, with minor proportions of goethite.

**Table 1.** Chemical composition of the sinter feed sample used in this study.

| Component | Fe | $SiO_2$ | $Al_2O_3$ | P | Mn | Loss on Ignition |
|---|---|---|---|---|---|---|
| % | 56.85 | 14.42 | 1.50 | 0.053 | 0.170 | 2.18 |

The interaction of the samples with two contact surfaces that represent wear materials that are widely used in the minerals industry for lining transfer chutes was studied. These were ASTM A532 II chrome carbide alloy [56], hereby identified as "Cast iron", and 92% alumina, identified as "Ceramic".

### *2.3. Bench-Scale Tests*

The bench-scale tests used were selected based on their ability to characterize the interaction of the material particles with each other as well as with the surface, under either nearly static or dynamic conditions. These tests are presented only briefly. More details of each test may be found as part of the Brazilian standard NBR 17177 [57], which was established based on the present work.

#### 2.3.1. Inclined Plane Test

The inclined plane test (Figure 2a) is used to determine the sliding angle of the ore in relation to a particular surface, and is suitable for assessing the interaction of the sample with a given surface. When coarser particles are to be analyzed, they may be placed either individually, directly on top of the surface [26], or with a layer of particles, without stacking [58]. Given the fine size of the sample, the test consisted of placing each sample of the ore in contact with a flat plate filling a void shallow container of 88 mm in diameter and 30 mm in height (top view shown in detail in Figure 2a), which was initially positioned horizontally. Slowly, the plate was inclined until the ore began to slide against the contact surface, at which point the slope of the plate was measured. The response of the ore was analyzed as a single mass [59].

The device built for the inclined plane test was activated by a linear actuator, which enables a description of the inclined plane's movement. Moreover, since the dimensions of the device are known, it is possible to determine the slope of the plane throughout the test from recordings using a Sony DSC-RX10 IV (Tokyo, Japan) digital camera. Parameters such as the static friction coefficient and the rolling friction of the ore with the surface are typically able to describe this interaction.

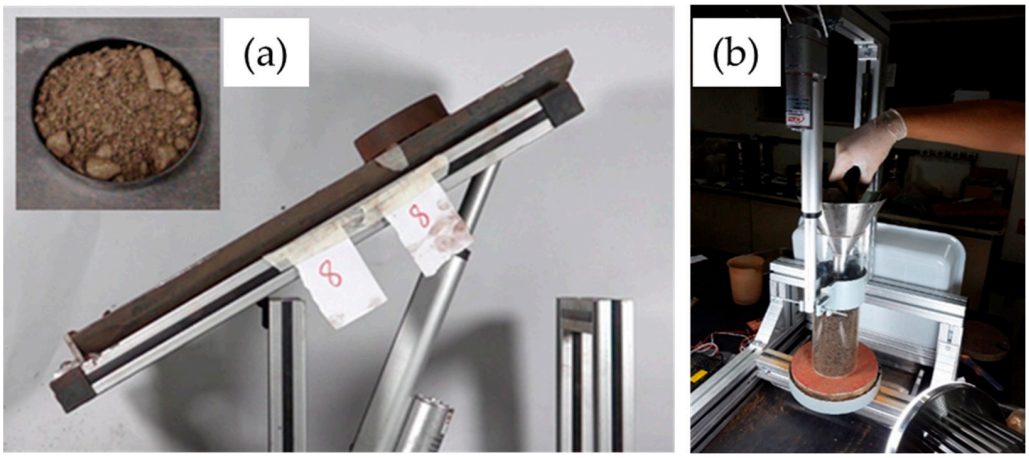



**Figure 2.** Test device with an inclined plane and container filled with sample (inset) (**a**), and device constructed to carry out the slump test (**b**).

#### 2.3.2. Slump Test

The slump test can be used to determine the static repose angle of the ore. Similarly to other pile formation tests proposed for several bulk materials, cohesive or not [7,28,58,60], in this test, a hollow cylinder filled with ore is placed over a horizontal surface. The pile is formed once the tube moves vertically. The angle between the side of the pile and the horizontal direction defines the repose angle [61]. This test can successfully capture the internal resistance of the material to flow under nearly static conditions, being marginally influenced by interactions with the material used for the surface.

In this test, a device (Figure 2b) that automatically raises the tube containing the ore at a constant rate (20 mm/s) using a step motor is used, minimizing human interference in the results of the test. A 200 mm diameter disc-shaped base is used for the deposition of the ore pile, which is positioned in such a way that excess material can flow outside of it, ensuring that the base of the pile has a constant diameter throughout the different tests. Additionally, to test the interaction of the ore with different surfaces, ceramic and cast iron discs were used.

The pile formed on the disk surface was photographed from various angles and, with the aid of image analysis software, its outline could be obtained.

#### 2.3.3. Drawdown Test

One additional measurement from the handling tests is the material's drained angle of repose [46], also known as the drawdown angle. This angle is formed by the ore after the flow of part of its pile, whether through side walls [59] or through gates positioned in the center [7,29] or on the sides [62] of acrylic boxes. This is considered the most comprehensive bench test as it provides various data about the dynamic behavior in ore flows, in addition to repose and drawdown angles, such as bin discharge, arch formation in their upper chamber, and mass flow, at a relatively low computational cost [22,23,40,62].

The test involves feeding an iron ore sample to the top of the device, followed by quick release of a gate at the bottom of the box (Figure 3a,b). The material, dropped under gravity, is directed to an obstacle represented by a flat plate on which a contact surface of interest can be set—this was ceramic or cast iron in the present work. Therefore, this is yet another test that can assess the interaction of the ore with several contact surface materials. Additionally, the slope of the obstacle can be varied to reproduce different wall angles commonly found in industrial transfer chutes. This makes it particularly suitable for capturing the interaction effects of the iron ore with the liner surface under conditions

that approach those in the field. In addition to the drawdown angle, the masses of ore remaining in sections A and B of the device (Figure 3a,b) were also recorded.

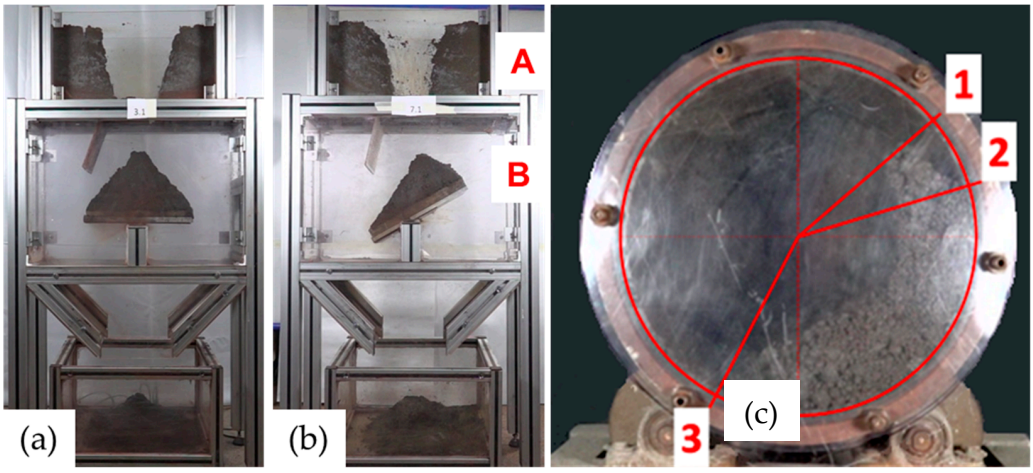



**Figure 3.** Device for dynamic handling testing (**a**,**b**). The plate underneath the trapdoor may be positioned horizontally (**a**) or inclined (**b**); tumbling test, highlighting (in red) the angular positions of the shoulder (1), the detachment (2), and the foot (3) (**c**).

#### 2.3.4. Tumbling Test

The tumbling test (Figure 3c) allows for the observation of the dynamic characteristics of the ore. This test involves filling a 305 mm diameter by 305 mm long laboratory drum with smooth steel walls (no lifter bars) with ore to a predetermined level, hereby set at 20%. The roughness of the internal surface, measured using Seimitsu E-35B (Tokyo, Japan), was 2.3 μm ± 0.8 μm, which is equivalent to that of the cast iron plate used in the previous tests (2.4 μm ± 0.6 μm). The drum is then sealed with an acrylic lid and set to rotate at a constant frequency. From the footage of the ore's movement, it is possible to determine the angular positions at which the ore "detaches" from the drum wall ("detachment"), rises after detachment ("shoulder"), and returns to contact with the wall ("foot") [22,26], as can be seen in Figure 3c. The angular positions were defined with respect to the axis of rotation of the cylinder, where the east, north, and south positions are 0°, 90°, and −90°, respectively. Angular positions were obtained through a visual inspection by trained technicians, using several sequential frames for one full rotation of the drum (60 frames). For convenience, foot angles are expressed as their absolute value. Tests were run at frequencies of 15 and 30 rpm.

### *2.4. Pilot-Scale Tests*

Pilot-scale tests were conducted using the Pilot Scale Handling Device (PSHD) (Figure 4). In these tests, ore is fed onto a conveyor belt with a 0.254 m (10″) width. The conveyor belt projects it against a rock box, allowing for the accumulation of material on its surface or against surface plates that are placed at different angles to reproduce typical wall angles in industrial transfer chutes. The ore then flows under gravity and exits the device through the discharge chute into a box. The area where the barrier is located is fitted with acrylic sidings to enable the visualization and recording of the test.

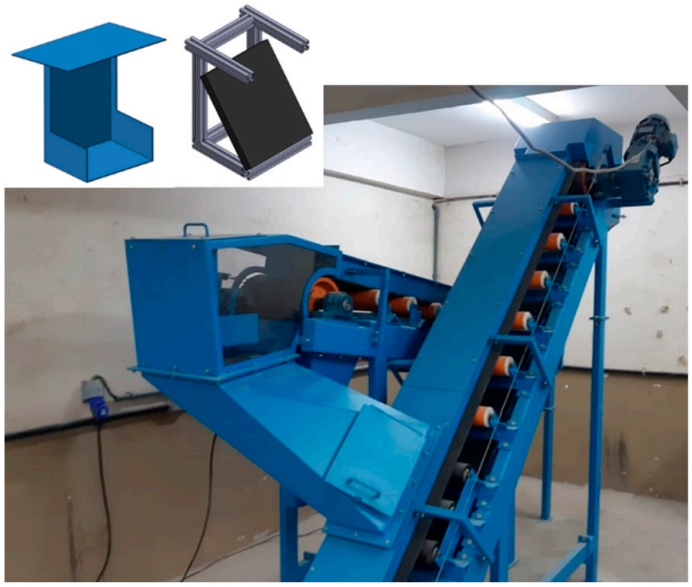


**Figure 4.** Pilot-scale handling device (PSHD) installed at the *Laboratório de Tecnologia Mineral* of the *Universidade Federal do Rio de Janeiro*. Inset shows the different impact systems.

The main objective of the pilot-scale tests was to verify the calibrated material and contact parameters, which were previously selected based on the bench-scale tests and, therefore not directly used for calibration. Tests were conducted using the rock box with three belt speeds, namely, 1, 2, and 3 m/s, and with inclined plates at angles of 32°, 37°, and 42°, with respect to the horizontal plane at 2 m/s. Validation was carried out through a visual inspection of flow in the discharge point, in addition to measurement of the mass accumulated in the rock box or on top of the contact surface upon completion of the test.

### *2.5. DEM Environment*

In DEM, simulations reproducing experiments, whether at the bench, pilot, or industrial scale, were carried out considering spherical particles of a single particle size (20 mm) to represent all the sinter feed samples. Although apparently simplistic, the use of a single sphere size was found to be necessary, given the need to conduct the simulation in no more than 24 h; for instance, when using industrial-scale transfer chutes fed with a rate as high as 20,000 t/h by an 213 cm (84 inch) belt with 4000 HP (2983 kW) of power in a shiploader with a 13 m drop height. Additionally, the shear modulus of particles and surfaces in DEM were set to $1 \times 10^8$ Pa, allowing for the use of larger time steps, whereas Poisson's ratio was set to 0.25 for all materials. The specific gravity of the ore sample was calibrated by reproducing the bulk density test in the DEM environment to reach a mass/volume ratio equivalent to those obtained in the experiment.

The calibration test simulations were replicated in a virtual environment using the commercial software EDEM™ (version 2022, Altair Engineering Inc., Troy, MI, USA), Rocky DEM (version 4.2, Engineering Simulation and Scientific Software LTDA, Rio de Janeiro, Brasil) and Bulk Flow Analyst™ (version 18, Overland Conveyor Company, Lakewood, CO, USA), all of which employ the Discrete Element Method. The contact model used in the simulations included the Hertz model [41] for describing normal contact, the Mindlin model [42] for describing tangential contact, and either the JKR model [46] or the SJKR model [48], which are commonly used to model the mechanics of cohesive wet particulate systems, such as the moist iron ore in this study. The input parameters for this model included the surface energy parameter $\gamma$ in J/m$^2$ (JKR model) or the cohesion coefficient (SJKR), in addition to the coefficients of restitution (CoR), static friction (SFC), and rolling friction (RFC). These parameters must be selected for particle–particle contacts and for

particle–geometry contacts, totaling eight parameters to be calibrated. The rolling resistance models used in the simulations were Type A for EDEM, defined as standard rolling friction in the version 2022, and Type C for Rocky DEM version 4.2 [54,55].

Table 2 lists the main components of the contact models used in this work, along with their respective references in the literature in EDEM and Rocky implementations.

**Table 2.** Main equations for the contact models used in this work.

| Software | EDEM 2022 | Rocky 4.2 | Contact Parameters |
|---|---|---|---|
| Normal force | Hertzian Spring Dashpot [63] | Hertzian Spring Dashpot [63] | CoR/SFC |
| Tangential Force | No-slip—Mindlin [64] | Mindlin–Deresiewicz [42] | |
| Adhesive Force | JKR—Johnson et al. [46] | JKR—Johnson et al. [46] | $\gamma_{JKR}$ |
| Rolling friction | Standard—Type A [65] | Type C [55] | RFC |

The approach used when estimating the optimal parameters consisted of running DEM simulations using a mixed-level full-factorial design. It initially involved exhaustively testing all combinations of the eight contact model parameters at the set levels shown in Table 3. Such a design was useful to represent both particle–particle and particle–surface contacts, resulting in a total of 36,864 simulations with the different combinations of parameters for each test in the case of EDEM, with 50 additional simulation cases from parameter expansions around selected points.

**Table 3.** Factor levels of particle–particle and particle–geometry contact parameters in the factorial design of simulations.

| Restitution—CoR | $\gamma_{JKR}$ (J/m²) | Static Friction—SFC | Rolling Friction *—RFC |
|---|---|---|---|
| 0.1 | 0 | 0.1 | 0.05 |
| 0.3 | 0.5 | 0.3 | 0.2 |
| 0.5 | 1.5 | 0.5 | 0.4 |
| - | 3.0 | 0.7 | 0.6 |

* Rocky requires only one rolling friction parameter for particle–particle or particle–geometry contacts, which reduces the number of parameters that require calibration to seven.

All parameter combinations were tested through simulations of the four bench-scale tests (Section 2.3) and evaluated based on their metrics. The overall objective function was composed of individual objective functions, ranging from one or two for each test. The objective function for the repose angle of a given set of parameters $k$ and experiment $j$ was calculated from $f_{1.k.j} = f^*_{1k,j} / \max\left(f^*_{1,k=1,..,n,j}\right)$, where the components are given by the following:

$$f^*_{1,kj} = h_1 \left| h_{j,exp} - h_{k,sim} \right| + \frac{1}{8} \sum_{l=1}^{8} s\left(A^l_{j,exp},\ A_{k,sim}\right) \quad (1)$$

where $h$ is the pile height and $s$ the average overlap area. $h_1$ is a scaling factor, which is arbitrarily set to 20, whereas $s$ is the pile overlap area, defined by the area represented by region $R^k$ (Figure 5), which is given by the following:

$$R^k = A_{exp} \cup A^k_{sim} - A_{exp} \cap A^k_{sim} \quad (2)$$

The overlap area $s$ is calculated from eight perspectives using the cardinal and intercardinal positions around the pile (Figure 5b). This approach was chosen to avoid the biased repose angle measurements obtained from simulations often found in rounded or flat piles.

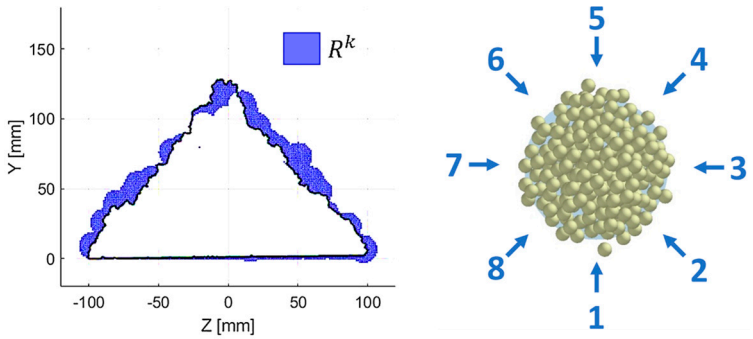



**Figure 5.** Projection of ore pile overlap (**a**) and the eight view planes for an analysis of the simulation of the angle in the repose test (**b**).

The sliding angle function ($f_2$) is calculated from $f_2 = \frac{1}{\theta_{max}}\left|\theta_{exp} - \theta_{sim}\right|$, where the value of the denominator $\theta_{max}$ refers to the maximum angle obtained in the experiments, which is equal to 60°, whereas $\theta_{exp}$ and $\theta_{sim}$ are the sliding angles obtained in the experiments and simulations, respectively.

Since the tumbling tests were performed at two different rotation frequencies (15 and 30 rpm), the objective functions $f_3$ and $f_4$ are defined as $f_3 = f_4 = \left(\left|\theta^{ft}_{exp} - \theta^{ft}_{sim}\right| + \left|\theta^{de}_{exp} - \theta^{de}_{sim}\right|\right)$, where $\theta$ is the angular position (Figure 3c) and the superscript refers to foot and detachment angles.

Finally, the drawdown experiments required two objective functions, $f_5$ and $f_6$. Functions $f_5$ and $f_6$ relate to the mass retained in the upper section ($m^A$) and in the midsection of the device, resting over the plate ($m^B$) 3.5 s after the opening of the hatch:

$$f_5 = f_6 = \left(\left|m^A_{exp} - m^A_{sim}\right| + 2\left|m^B_{exp} - m^B_{sim}\right|\right) \quad (3)$$

Naturally, the results from each test may be fitted with a distinct set of parameters that best represent the test. However, to select the set of parameters that, on average, best represent the behavior of the ore in all tests, a weighed-averaged objective function ($f$) was proposed, which accounted for the results of each test ($f_1$) and their respective weights ($w_i$) through the following equation:

$$f = \frac{\sum_{i=1}^{N} w_i f_i}{\sum_{i=1}^{N} w_i} \quad (4)$$

where the weights, selected by trial and error, are listed in Table 4.

**Table 4.** Arbitrary weights used in the objective function for each test, defined by Equation (4).

| Test | Objective Function | Weight |
|---|---|---|
| Repose angle | $f_1$ | 1 |
| Sliding angle | $f_2$ | 3 |
| Tumbling (15 rpm) * | $f_3$ | 0.002 |
| Tumbling (30 rpm) * | $f_4$ | 0.002 |
| Drawdown (horizontal) | $f_5$ | 0.007 |
| Drawdown (30°) | $f_6$ | 0.007 |

* Available only for cast iron.

The five most suitable sets of parameters defined using this approach were then used in simulations of the pilot-scale device.

In order to maintain consistency in the particle–particle parameters and owing to the larger set of tests available in the case of cast iron, a hierarchical approach was used. The optimal contact parameters were first selected using the data for cast iron. After the

optimal parameters were selected, the particle–particle parameters were maintained and only the particle–surface parameters were varied to match the results from tests involving the ceramic surface.

On the other hand, as the contact model implemented in the software Bulk Flow Analyst is different from the models used in the other two software, factorial simulations were not carried out. An expedite calibration procedure was performed using this software. This was based on prior experience with this software when used for simulations of transfer chutes for the virtual reproduction of bench- and pilot-scale tests.

### *2.6. Industrial-Scale Tests*

As a full-scale validation, an industrial chute that operates in a port facility was selected (Figure 6). The system was designed for handling iron ore with bulk density of up to 3.5 t/m$^3$ at a maximum rate of 10,000 t/h (2857 m$^3$/h) and a nominal rate of 8000 t/h (2286 m$^3$/h) between two 152 cm (60 inch) wide conveyor belts operating at a fixed speed of 3.3 m/s. The drop height from the top of the pulley to the receiving belt was 4 m. Simulations were carried out with constant flows using the same ore that was used in the other scale tests. Simulation results were compared qualitatively with historical operation and maintenance events, such as instances of misalignment or blockages, and other occurrences.

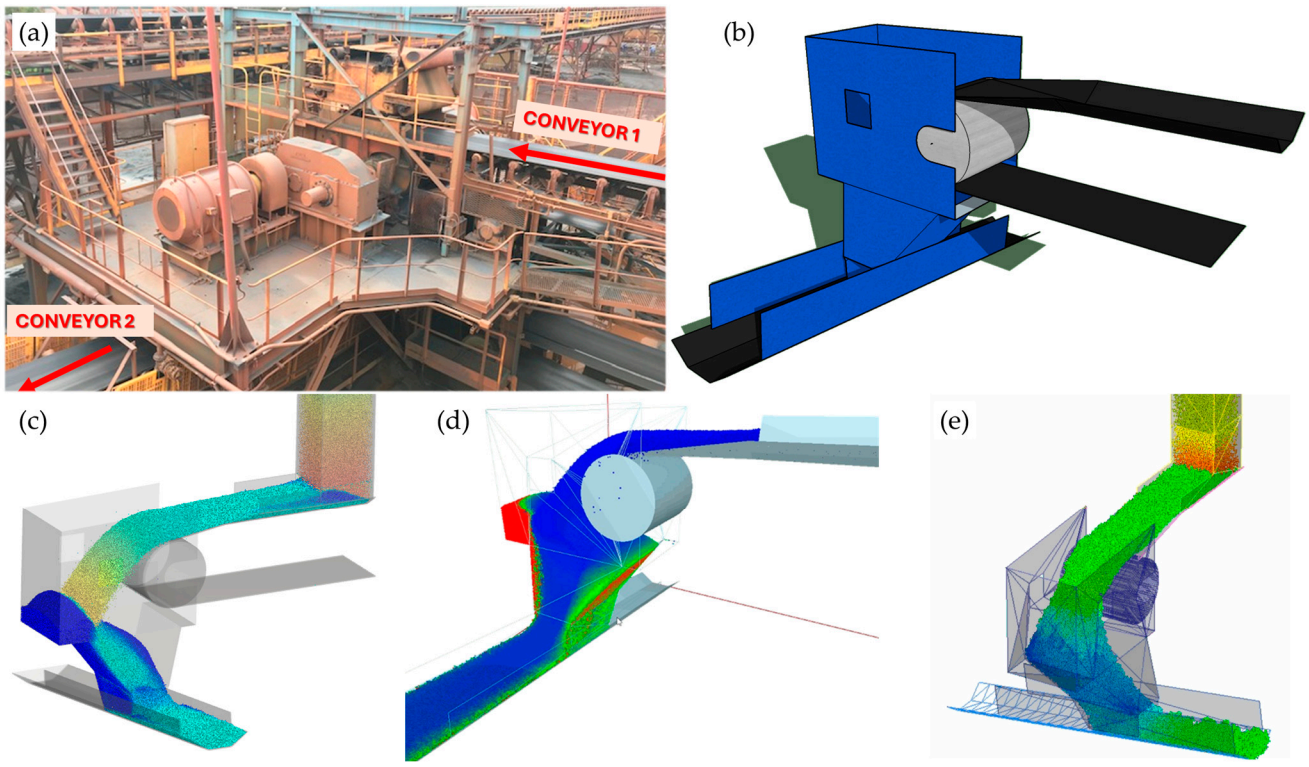



**Figure 6.** Industrial-scale transfer chute from a port terminal (**a**), constructed three-dimensional model (**b**), flow simulation using Rocky DEM (**c**), using EDEM® (**d**), and using Bulk Flow Analyst (**e**).

## 3. Results and Discussion

### *3.1. Bench-Scale Test Results*

The bulk density of the sample was 2141 ± 46 kg/m$^3$, which resulted in a solids density of 3880 kg/m$^3$ for the 20 mm spherical particles that were simulated.

A summary of results from the bench-scale tests is presented in Table 5. It is evident that some tests were more sensitive to the contact surface than others. Indeed, no statistical differences (*t*-test with a significance of 0.05) between the repose angles obtained in the pile

formation (slump) test and the masses obtained in both the feeding and the inclined plates in the dynamic handling (drawdown) test were found for the different tested surfaces.

**Table 5.** Summary of results from the bench-scale experiments.

| Test | Measurement | Surface | | | |
|---|---|---|---|---|---|
| | | Cast Iron | | Ceramic | |
| | | Mean | Standard Deviation | Mean | Standard Deviation |
| Slump | Repose angle (°) | 52.6 | 3.5 | 49.3 | 3.7 |
| Inclined angle | Sliding angle (°) | 36.1 | 1.6 | 33.7 | 1.9 |
| Drawdown | Mass on top section (%) | 62.64 | 2.32 | 62.64 | 2.32 |
| Drawdown | Mass on inclined plate (%) | 16.24 | 0.36 | 13.93 | 0.09 |
| Tumbling (15 rpm) | Foot angle (°) | 112 | 1 | - | - |
| Tumbling (15 rpm) | Detachment angle (°) | 15 | 1 | - | - |
| Tumbling (30 rpm) | Foot angle (°) | 114 | 1 | - | - |
| Tumbling (30 rpm) | Detachment angle (°) | 18 | 1 | - | - |

On the other hand, the results from Table 5 confirm a common observation in industry: that ceramic plates allow for better material flow compared to metallic plates, as evidenced by the lower sliding angle in the inclined angle test and the lower material mass on the inclined plate of the drawdown test. An analysis of the tumbling tests, which were available only for the cast iron parameter calibration, showed that the foot and detachment angle slightly increased with an increased rotation frequency.

A sensitivity analysis of the outcomes from the tests with varying contact parameters is shown in Figure 7 for EDEM. This shows that the objective function $f_1$ yields minimal values when particle–particle static friction and JKR coefficients had intermediate values. Simulation with optimal values resulted in a repose angle of 52°.

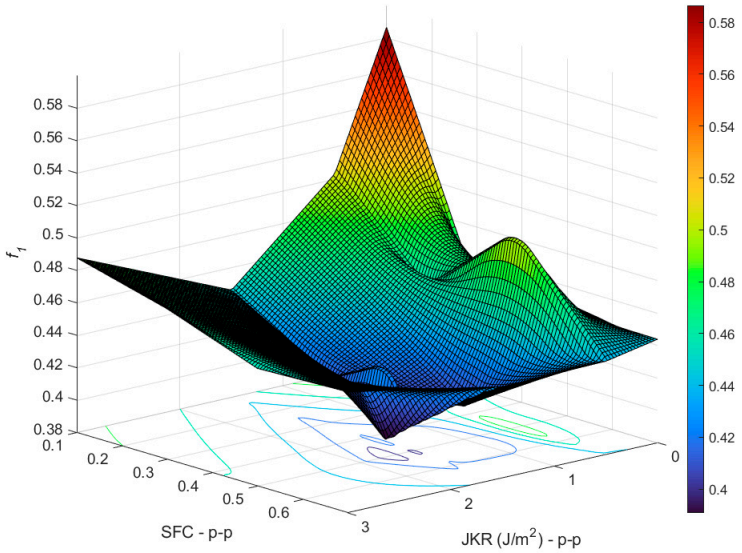



**Figure 7.** Response surface showing the effects of particle–particle static friction (SFC) and $\gamma_{JKR}$ coefficients on the objective function $f_1$ from the repose angle test for the sinter feed sample and cast iron sample. In the figure, the coefficients of restitution and rolling friction were set to 0.3 and 0.2 for particle–particle contacts, whereas $\gamma_{JKR}$, restitution, static friction, and rolling friction coefficients for particle–surface contacts were set to 0.0, 0.1, 0.7, and 0.6, respectively.

Replication of the bench-scale tests in a virtual environment (Figure 8) allowed for the selection of five parameter sets that best represented the combined effects of the tests in EDEM and Rocky. For illustration purposes, the five most suitable parameter

sets from the bench-scale tests with a cast iron surface are listed in Table 6 for EDEM, along with their respective objective function values. Coincidently, the best sets presented the same particle–particle rolling and particle–surface static friction coefficient values. On the other hand, the surface energy parameter ($\gamma_{JKR}$) varied from 0.5 to 3.0 in the case of particle–particle contacts. A single occurrence of 3.0 J/m$^2$ was found for the particle–surface contacts among the other four cohesionless parameter sets.

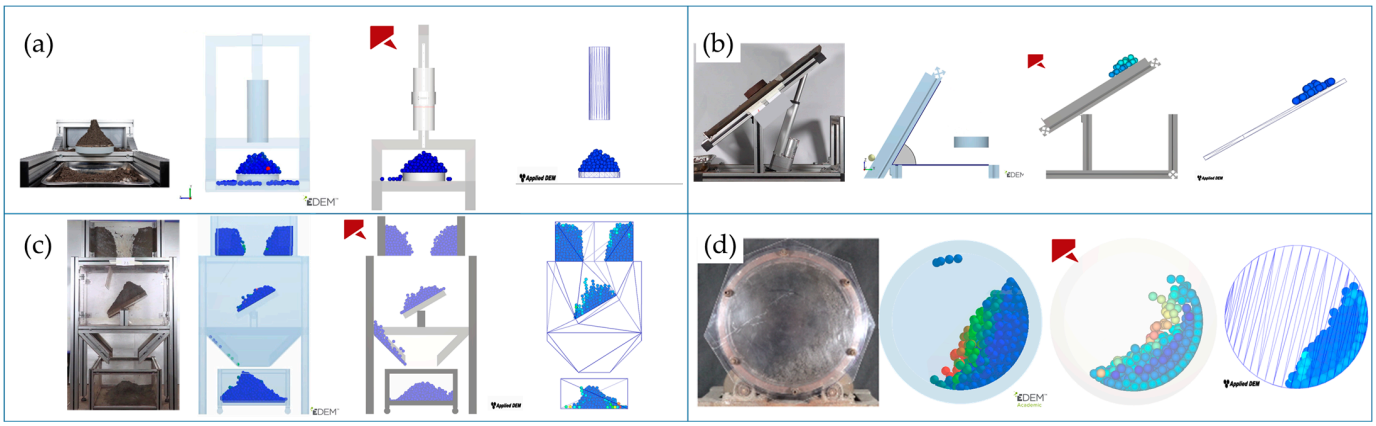



**Figure 8.** Reproduction of selected bench tests in a virtual environment with different software: slump (**a**), inclined plane (**b**), drawdown angle (**c**), and tumbling (**d**).

**Table 6.** Five most suitable sets of calibrated contact parameters for cast iron surface in Altair EDEM.

| Simulation Number | Particle–Particle | | | | Particle–Cast Iron | | | | Objective Function—$f$ (-) | Mass on Plate (kg) * |
|---|---|---|---|---|---|---|---|---|---|---|
| | $\gamma_{JKR}$ (J/m$^2$) | CoR (-) | SFC (-) | RFC (-) | $\gamma_{JKR}$ (J/m$^2$) | CoR (-) | SFC (-) | RFC (-) | | |
| 21,459 | 3.00 | 0.50 | 0.30 | 0.00 | 3.00 | 0.50 | 0.70 | 0.40 | 0.487 | 0.00 |
| 36,867 | 1.75 | 0.30 | 0.50 | 0.94 | 0 | 0.10 | 0.70 | 0.60 | 0.506 | 0.94 |
| 21,477 | 1.50 | 0.30 | 0.50 | 1.50 | 0 | 0.10 | 0.70 | 0.60 | 0.515 | 1.50 |
| 36,881 | 1.50 | 0.30 | 0.50 | 1.84 | 0 | 0.10 | 0.70 | 0.65 | 0.520 | 1.84 |
| 36,908 | 0.50 | 0.50 | 0.30 | 1.28 | 0 | 0.50 | 0.70 | 0.60 | 0.520 | 1.28 |

* Pilot-scale test with cast iron surface inclined at 32°.

### *3.2. Pilot-Scale Tests*

In the tests conducted at a belt speed of 1 m/s, the momentum was insufficient for the ore to reach the rock box. Tests at speeds of 2 m/s (Figure 9a) and 3 m/s (Figure 9c) resulted in the accumulation of mass in the rock box. Additionally, Figure 9e,g shows evidence of accumulation of mass on top of ceramic and cast iron plates angled at 32° with respect to the horizontal plane, equal to 0.22 kg and 2.55 kg, respectively. Tests with plates at steeper angles (37° and 42°) did not result in any measurable material accumulation.

Simulations of the pilot-scale tests were run with the different sets of parameters obtained from the bench-scale tests (Table 6) and the mass of material deposited on the inclined plate was recorded; these results are also presented in the table. It is evident that the predictions varied significantly, with simulation 36,881 approaching the measured value of 2.55 kg recorded during the test. As such, although all five parameter sets presented in Table 6 could sufficiently reproduce the behavior of the material in the collection of bench-scale tests used in this work, some of them failed to reproduce the behavior observed in the pilot-scale tests. Indeed, the selected test was not the one with the lowest objective function value, further demonstrating the value of the multiscale parameter selection approach.

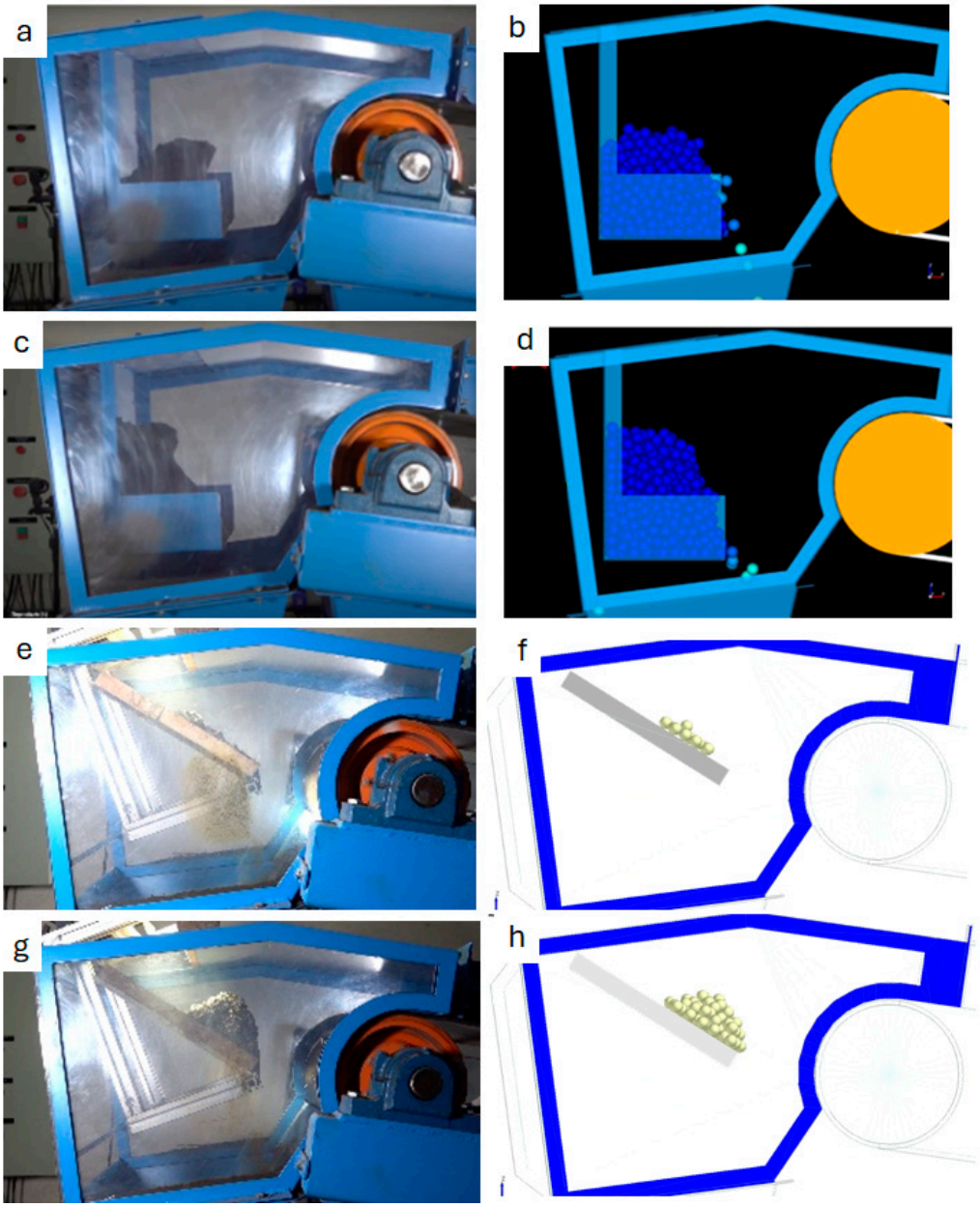



**Figure 9.** Pilot-scale tests and their respective simulations with projection speeds of 2 m/s (**a**,**b**) and 3 m/s (**c**,**d**) against the rock box, against a 32° ceramic plate (**e**,**f**), and against a 32° cast iron plate (**g**,**h**).

Visually, the accumulated material in the rock box for the optimal set closely resembled the simulated results based on these optimal parameters (Figure 9).

Following the hierarchical approach, the five sets of parameters for the ceramic plate were obtained from the bench-scale tests, selecting particle–particle parameters previously obtained using the cast iron tests (case 36,881) and identifying those that exhibited the lowest objective function values (Table 7). Similarly, simulations of the pilot-scale tests were then carried out and the one that most closely matched the mass retained on the ceramic plate angle 32° was case 33,886, with 0.18 kg. This set presented a lower particle–surface rolling friction coefficient when compared to the optimum case for cast iron (Table 6) when the predictions were compared to the experiment in Figure 9f. The same approach was used for Rocky DEM, and the results are presented in the Appendix A.

**Table 7.** Response of five most suitable sets of calibrated contact parameters for the iron ore with the ceramic plate.

| Simulation Number | Particle–Particle | | | | Particle–Cast Iron | | | | Objective Function—$f$ (-) | Mass on Plate * (kg) |
|---|---|---|---|---|---|---|---|---|---|---|
| | $\gamma_{JKR}$ (J/m$^2$) | CoR (-) | SFC (-) | RFC (-) | $\gamma_{JKR}$ (J/m$^2$) | CoR (-) | SFC (-) | RFC (-) | | |
| 36,887 | 1.50 | 0.30 | 0.50 | 0.20 | 0.00 | 0.10 | 0.70 | 0.55 | 0.430 | 0.63 |
| 36,907 | 1.50 | 0.30 | 0.50 | 0.20 | 0.00 | 0.10 | 0.70 | 0.60 | 0.431 | 1.50 |
| 36,881 | 1.50 | 0.30 | 0.50 | 0.20 | 0.00 | 0.10 | 0.70 | 0.65 | 0.456 | 1.84 |
| 36,886 | 1.50 | 0.30 | 0.50 | 0.20 | 0.00 | 0.10 | 0.70 | 0.45 | 0.456 | 0.18 |
| 36,882 | 1.50 | 0.30 | 0.50 | 0.20 | 0.00 | 0.10 | 0.70 | 0.50 | 0.496 | 0.53 |

* Pilot-scale test with ceramic surface inclined at 32°.

A summary of the sets of contact parameters selected for each software is listed in Table 8. The differences found between some of the parameters in the different simulators may be associated with differences in the rolling friction models´ implementation. Calibration on EDEM and Rocky allowed for discrimination between contact surfaces: while EDEM only required changes in the particle–surface rolling friction, Rocky demanded the use of different particle–particle parameters. Calibration using Bulk Flow Analyst was performed regardless of the surface material used, since the software limits the degrees of freedom of the contact models that are implemented.

**Table 8.** Sets of selected calibrated contact parameters.

| Software | Lining Surface | Particle–Particle | | | | Particle–Geometry | | | |
|---|---|---|---|---|---|---|---|---|---|
| | | JKR (J/m$^2$) | Restitution | Static Friction | Rolling Friction | JKR (J/m$^2$) | Restitution | Static Friction | Rolling Friction |
| EDEM | Cast iron | 1.50 | 0.30 | 0.50 | 0.20 | 0 | 0.10 | 0.70 | 0.65 |
| EDEM | Ceramic | 1.50 | 0.30 | 0.50 | 0.20 | 0 | 0.10 | 0.70 | 0.45 |
| Rocky | Cast iron | 0 | 0.10 | 0.70 | 1.00 | 0 | 0.10 | 0.70 | 1.00 |
| Rocky | Ceramic | 0.50 | 0.10 | 0.70 | 0.80 | 0.50 | 0.10 | 0.30 | 0.80 |
| BFA | - | 0.30 * | - | 0.30 | - | 0.03 * | - | 0.60 | - |

* SJKR parameter in (J/m$^3$).

### *3.3. Industrial Chute Validation*

Anecdotal evidence of the chute in question suggests that blockages occur when the chute is operating with this sinter feed ore at a rate of 10,000 t/h and that safe operation is possible at 5000 t/h. In order to assess the simulations' ability to predict these scenarios, the total mass of particles accumulated in the system was recorded. Figure 10a shows that it was not possible to achieve steady-state conditions at a flowrate of 10,000 t/h, indicating blockages in the chute in agreement with industrial observations, whereas Figure 10b shows that steady-state conditions were reached in the simulation, with a maximum mass of accumulated material of 8 t at a feed rate of 5000 t/h. It is evident in Figure 10a that the predictions from Bulk Flow Analyst were more pessimistic than those made with the other software.

Figure 11 compares ore flow predictions when the chute was operating with ceramic and cast iron plates at 10,000 t/h. It shows that, although also unable to reach steady-state conditions, the operation with ceramic plates was able to delay, however slightly, the onset of blockage, especially for simulations performed in Rocky DEM. The higher sensitivity to the surface material obtained when using Rocky may be attributed to the Type C rolling friction model used in calibration. For instance, the current versions of EDEM use the Type C model, which will be evaluated in future work. In practice, it is known that ceramic plates are found to facilitate ore flow in chutes. Even if it does not reach the original design

rate, the chute under study could, potentially, operate at higher rates when handling sticky ores when ceramic surfaces are used compared to surfaces with cast iron.

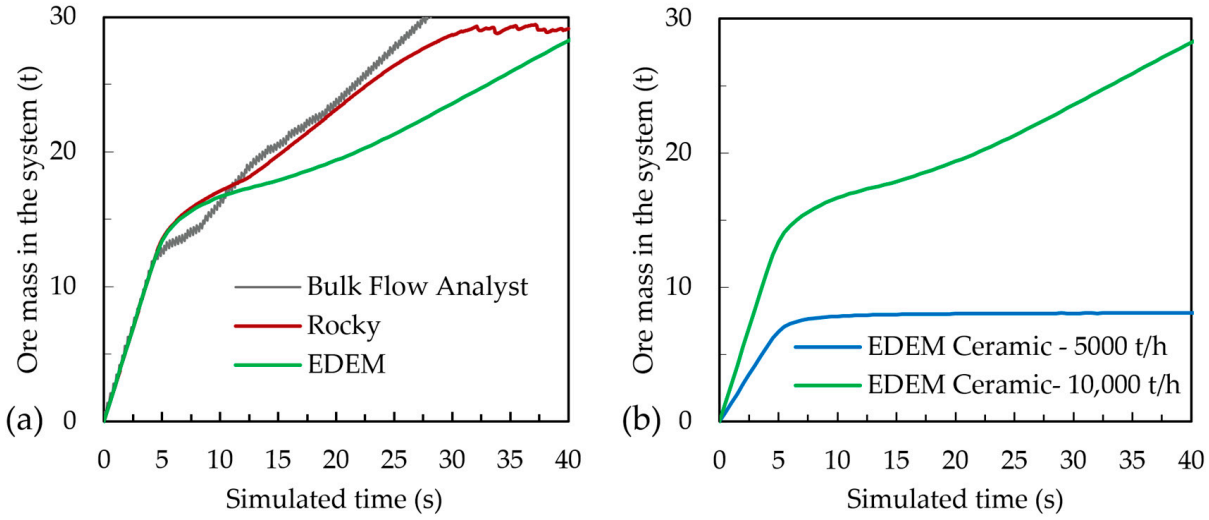



**Figure 10.** Accumulated mass in the chute shown in Figure 6 at a rate of 10,000 t/h using Rocky DEM, Altair EDEM®, and Bulk Flow Analyst (**a**), and at rates of 5000 t/h and 10,000 t/h using EDEM (**b**) with the chute with ceramic lining.

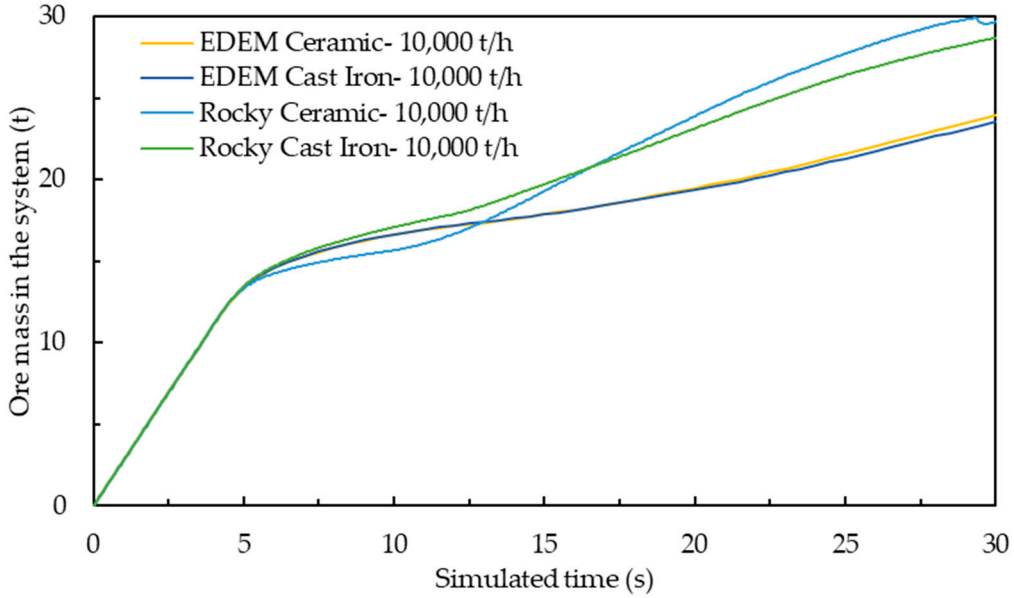



**Figure 11.** Accumulated mass in the chute show in Figure 6 with different contact surfaces at 10,000 t/h, predicted using Rocky and EDEM.

Further, a closer examination was conducted of the discharge of the ore onto the receiving belt, which is relevant from a maintenance perspective. Figure 12 demonstrates that, at both operating rates, the material was delivered quite centrally, which supports the anecdotal evidence of the absence of equipment failure history related to belt misalignment due to off-center material discharge, resulting in average mass distributions of 49.1% and 49.5% on the left half of the belt for 5000 and 10,000 t/h operating rates, respectively.

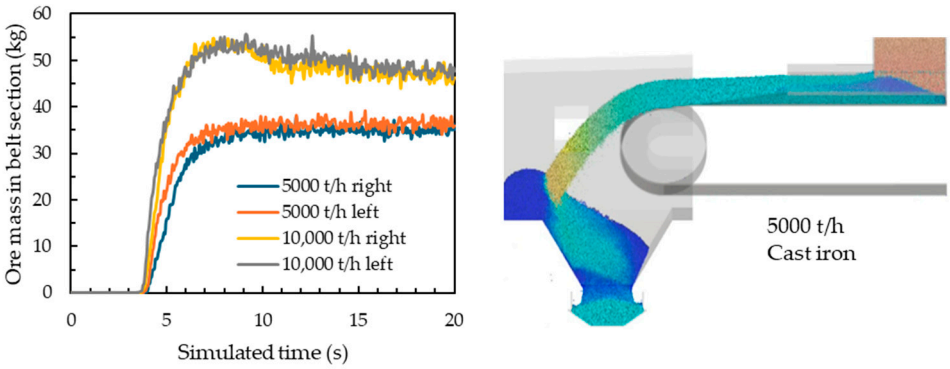



**Figure 12.** Assessment of load centralization on the belt at rates of 5000 t/h and 10,000 t/h.

## 4. Conclusions

By combining various bench-scale tests, some of which were more sensitive to certain parameters than others, it was possible to obtain well-calibrated parameter sets that are suitable for a sinter feed sample with a fixed moisture content interacting with two contact surfaces (ceramic and cast iron).

Pilot-scale tests were then used to select the optimal parameter sets through a comparison of the mass accumulated in an inclined plate to the simulations. Good agreement was found between the test results and simulations using different commercial software, even with the study's constraint of using spherical particles that are significantly coarser than those making up the sinter feed, showing the robustness of the calibration procedure.

Simulations of the operation of an industrial-scale chute confirmed the validity of the calibrated parameters, since they were able to predict blockage at 10,000 t/h and normal operation at 5000 t/h, as well as showing that the use of ceramic lining delayed blockage when operating at 10,000 t/h, particularly in the case of Rocky using the Type C rolling friction model. Finally, the simulations showed that the assessed chute configuration was able to deliver a balanced load on the receiving conveyor belt, showing an agreement with the anecdotal evidence.

In spite of its limitations and the risk of developing shear planes during material flow, the selection of spherical particles with a 20 mm diameter in the simulations proved to be a viable choice, allowing for quick simulation execution within 24 h, which provides chute operators with enough time to take countermeasures in their daily operations. Indeed, comparative simulations were carried out where the material was within a narrow size range (18–22 mm), with no differences observed, but these required nearly 50% more computational effort. This demonstrated that, for the simulated conditions, shear planes did not result from the single-size simulations.

The multi-scale approach used in the present work, through which selected sets of contact parameters were identified based on bench-scale tests and the most suitable set was selected from pilot-scale tests, was shown to allow for realistic simulations of the industrial chute of interest. This may be a valid option in the case of materials with complex cohesive behavior, but is not necessarily critical for free-flowing materials, which are well-known to rely on estimates from bench-scale tests.

**Author Contributions:** Conceptualization, R.M.d.C. and L.M.T.; methodology, R.M.d.C. and G.P.d.O.; software, R.M.d.C. and H.P.d.S.A.; validation, G.P.d.O.; formal analysis, G.P.d.O. and H.P.d.S.A.; investigation, R.M.d.C. and G.P.d.O.; resources, G.P.d.O. and L.M.T.; data curation, R.M.d.C. and G.P.d.O.; writing—original draft preparation, R.M.d.C. and G.P.d.O.; writing—review and editing, R.M.d.C., G.P.d.O. and L.M.T.; visualization, G.P.d.O.; supervision, R.M.d.C. and L.M.T.; project administration, L.M.T.; funding acquisition, R.M.d.C., G.P.d.O. and L.M.T. All authors have read and agreed to the published version of the manuscript.

**Funding:** This research was partially funded by FAPERJ, grant number E-26/202.814/2019 and CNPq—Conselho Nacional de Desenvolvimento Científico e Tecnológico, grant number 313222/2021-5 and Coordenação de Aperfeiçoamento de Pessoal de Nível Superior—Brasil (CAPES)—Finance Code 001.

**Data Availability Statement:** The datasets generated during and/or analyzed during the current study are available from the corresponding author on reasonable request.

**Acknowledgments:** The authors would like to thank the technical team from Universidade Federal do Rio de Janeiro for performing the experiments.

**Conflicts of Interest:** The authors declare no conflicts of interest.

## Appendix A

**Table A1.** Response of five most suitable sets of calibrated contact parameters for pilot-scale simulations with a 32° cast iron plate in Rocky.

| Simulation Number | Particle–Particle | | | | Particle–Cast Iron | | | | Objective Function—$f$ (-) | Mass on Plate (kg) |
|---|---|---|---|---|---|---|---|---|---|---|
| | $\gamma_{JKR}$ (J/m$^2$) | CoR (-) | SFC (-) | RFC (-) | $\gamma_{JKR}$ (J/m$^2$) | CoR (-) | SFC (-) | RFC (-) | | |
| 1872 | 3.0 | 0.3 | 0.3 | 1.0 | 0 | 0.1 | 0.7 | 1.0 | 0.068 | 3.15 |
| 1167 | 1.5 | 0.1 | 0.5 | 0.8 | 0 | 0.1 | 0.7 | 0.8 | 0.069 | 2.36 |
| 1168 | 1.5 | 0.1 | 0.5 | 1.0 | 0 | 0.1 | 0.7 | 1.0 | 0.070 | 2.05 |
| 0208 | 0 | 0.1 | 0.7 | 1.0 | 0 | 0.1 | 0.7 | 1.0 | 0.074 | 2.55 |
| 1678 | 3.0 | 0.1 | 0.5 | 0.6 | 0 | 0.1 | 0.7 | 0.6 | 0.076 | 1.63 |

**Table A2.** Response of five most suitable sets of calibrated contact parameters for pilot-scale simulations with a 32° ceramic plate in Rocky.

| Simulation Number | Particle–Particle | | | | Particle–Cast Iron | | | | Objective Function—$f$ (-) | Mass on Plate (kg) |
|---|---|---|---|---|---|---|---|---|---|---|
| | $\gamma_{JKR}$ (J/m$^2$) | CoR (-) | SFC (-) | RFC (-) | $\gamma_{JKR}$ (J/m$^2$) | CoR (-) | SFC (-) | RFC (-) | | |
| 1678 | 3.0 | 0.1 | 0.5 | 0.6 | 0 | 0.1 | 0.7 | 0.6 | 0.298 | 1.63 |
| 1167 | 1.5 | 0.1 | 0.5 | 0.8 | 0 | 0.1 | 0.7 | 0.8 | 0.301 | 2.36 |
| 0727 | 0.5 | 0.1 | 0.7 | 0.8 | 0.5 | 0.1 | 0.3 | 0.8 | 0.303 | 0.37 |
| 0208 | 0.0 | 0.1 | 0.7 | 1.0 | 0 | 0.1 | 0.7 | 1.0 | 0.305 | 2.55 |
| 1168 | 1.5 | 0.1 | 0.5 | 1.0 | 0 | 0.1 | 0.7 | 1.0 | 0.305 | 2.05 |

## References

1. CEMA. *Belt Conveyors for Bulk Materials*, 7th ed.; CEMA: Bonita Springs, FL, USA, 2014.
2. Swinderman, R.T.; Marti, A.D.; Goldbeck, L.J.; Marshall, D.; Strebel, M.G. *Foundations™ The Practical Resource for Cleaner, Safer, More Productive Dust & Material Control*, 4th ed.; Martin Engineering Company: Neponset, IL, USA, 2009.
3. Benjamin, C.; Donecker, P.; Huque, S.; Rozentals, J. *The Transfer Chute Design Manual for Conveyor Belt Systems*; Conveyor Transfer Design Pty Ltd.: Spring Hill, QLD, Australia, 2015.
4. Gavi, J. *Solução em Transporte e Transferência de Materiais. Manual de Inspeção e Manutenção de Correias Transportadoras e seus Periféricos*, 1st ed.; Vitória: Bios Editoração, Brasil, 2011.
5. Cundall, P.A.; Strack, O.D.L. A discrete numerical model for granular assemblies. *Géotechnique* **1979**, *29*, 47–65. [CrossRef]
6. Kessler, F.; Prenner, M. DEM—Simulation of Conveyor Transfer Chutes. *FME Trans.* **2009**, *37*, 185–192.
7. Grima, A.; Hastie, D.; Curry, D.; Wypych, P.; Laroche, R. The Beginning of a New Era in Design: Calibrated Discrete Element Modelling. *Aust. Bulk Handl. Rev.* **2011**, *16*, 14–21.
8. Mason, A. Improved Transfer Chute Design Using DEM Software to Predict Material Flow Behavior. Bachelor of Engineering (Mechanical) Dissertation, University of Southern Queensland, Toowoomba, QLD, Australia, 2016.
9. Bharadwaj, R. Using DEM to Solve Bulk Material Handling Problems. *Chem. Eng. Prog.* **2012**, *108*, 54–58.
10. Ilic, D.; Donohue, T.J. On the Design and Analysis of Transfer Chute Systems. In Proceedings of the XXVI Encontro Nacional de Tratamento de Minérios e Metalurgia Extrativa, Poços de Caldas, Brazil, 18–22 October 2015.
11. Gröger, T.; Katterfeld, A. Discrete Element Simulation of Transfer Stations and Their Verification. *Bulk Solids Handl.* **2007**, *27*, 158–166.

12. Rossow, J.; Coetzee, C.J. Discrete element modelling of a chevron patterned conveyor belt and a transfer chute. *Powder Technol.* **2021**, *391*, 77–96. [CrossRef]
13. Coetzee, C.; Scheffler, O.C. Comparing particle shape representations and contact models for DEM simulation of bulk cohesive behaviour. *Comput. Geotech.* **2023**, *159*, 105449. [CrossRef]
14. Scheffler, O.C.; Coetzee, C. DEM calibration for simulating bulk cohesive materials. *Comput. Geotech.* **2023**, *161*, 105476. [CrossRef]
15. Katterfeld, A.; Donohue, T.; Ilic, D. Application of the Discrete Element Method in Mechanical Conveying of Bulk Materials. In Proceedings of the 7th International Conference for Conveying and Handling of Particulate Solids (CHoPS), Friedrichshafen, Germany, 10–13 September 2012.
16. Ilic, D.; Ariff, F.M.; Sommer, K.; Santos, M.; Yuming, D. Application of DEM to Blending and Homogeneity Evaluation and Improvement in a Belt Conveyor Transfer Chute System. In Proceedings of the Ninth World Conference on Sampling and Blending (WCSB), Beijing, China, 6–9 May 2019.
17. Weinhart, T.; Labra, C.; Luding, S.; Ooi, J.Y. Influence of coarse-graining parameters on the analysis of DEM simulations of silo flow. *Powder Technol.* **2016**, *293*, 138–148. [CrossRef]
18. Chu, K.; Chen, J.; Yu, A. Applicability of a coarse-grained CFD–DEM model on dense medium cyclone. *Miner. Eng.* **2016**, *90*, 43–54. [CrossRef]
19. Xu, L.; Wu, X.; Wang, S.; Bao, S. Multi-level coarse-grained discrete element method modeling of cylinder particle flow in a rotating drum. *Particuology* **2024**, *88*, 218–238. [CrossRef]
20. Lommen, S.; Mohajeri, M.; Lodewijks, G.; Schott, D. DEM particle upscaling for large-scale bulk handling equipment and material interaction. *Powder Technol.* **2019**, *352*, 273–282. [CrossRef]
21. Coetzee, C.J. Review: Calibration of the Discrete Element Method. *Powder Technol.* **2017**, *310*, 104–142. [CrossRef]
22. Coetzee, C.J.; Scheffler, O.C. The calibration of dem parameters for the bulk modelling of cohesive materials. *Processes* **2022**, *11*, 5. [CrossRef]
23. Carr, M.J.; Roessler, T.; Robinson, P.W.; Otto, H.; Richter, C.; Katterfeld, A.; Wheeler, C.A. Calibration procedure of Discrete Element Method (DEM) parameters for wet and sticky bulk materials. *Powder Technol.* **2023**, *429*, 118919. [CrossRef]
24. Liu, Z.; Yuan, J.; Shen, J.; Hu, Y.; Chen, S. A new DEM calibration method for wet and stick materials based on the BP neural network. *Powder Technol.* **2024**, *448*, 120228. [CrossRef]
25. Mohajeri, M.J.; Rhee, C.; Schott, D.L. Replicating cohesive and stress-history-dependent behavior of bulksolids: Feasibility and definiteness in DEM calibration procedure. *Adv. Powder Technol.* **2021**, *32*, 1532–1548. [CrossRef]
26. Barrios, G.K.P.; de Carvalho, R.M.; Kwade, A.; Tavares, L.M. Contact Parameter Estimation for DEM Simulation of Iron Ore Pellet Handling. *Powder Technol.* **2013**, *248*, 84–93. [CrossRef]
27. Roessler, T.; Katterfeld, A. Scaling of the angle of repose test and its influence on the calibration of DEM parameters using upscaled particles. *Powder Technol.* **2018**, *330*, 58–66. [CrossRef]
28. Rackl, M.; Hanley, K.J. A Methodical Calibration Procedure for Discrete Element Models. *Powder Technol.* **2016**, *307*, 73–83. [CrossRef]
29. You, Y.; Guo, J.; Li, G.; Lv, X.; Wu, S.; Li, Y.; Yang, R. Investigation the iron ore fine granulation effects and particle adhesion behavior in a horizontal high-shear granulator. *Powder Technol.* **2021**, *394*, 162–170. [CrossRef]
30. Mohajeri, M.J.; de Kluijver, W.; Helmons, R.L.; van Rhee, C.; Schott, D.L. A validated co-simulation of grab and moist iron ore cargo: Replicating the cohesive and stress-history dependent behaviour of bulk solids. *Adv. Powder Technol.* **2021**, *32*, 1157–1169. [CrossRef]
31. Ilic, D.; Roberts, A.; Wheeler, C. Modelling bulk solid interactions in transfer chutes: Accelerated flow. *Chem. Eng. Sci.* **2019**, *209*, 115197. [CrossRef]
32. Magalhães, M.F.; Chieregati, A.C.; Ilic, D.; de Carvalho, R.M.; Lemos, M.G.; Delboni, H., Jr. Use of Discrete Element Modelling to evaluate the parameters of the sampling theory in the feed grade sampler of a sulphide gold plant. *Minerals* **2021**, *11*, 978. [CrossRef]
33. Basu, S.; Chakrabarty, A.; Nag, S.; Behera, K.; Bandyopadhyay, B.; Grima, A.P.; Ghosh, P. Design modification of iron ore bearing transfer chute using discrete element method. *Eng. Comput.* **2021**, *38*, 3590–3607. [CrossRef]
34. Kumar, R.; Jha, P.K.; Kishore, R.; Singh, R.K.; Subrahmanyam, T.V.S.; Chaurasiya, S.K.; Mangipudi, K.R.; Sahu, K.K. Analysing the flow of wet iron ore in an industrial transfer chute using discrete element method. *Miner. Process. Extr. Metall.* **2024**, *133*, 131–146. [CrossRef]
35. Oliveira, G.P.; de Carvalho, R.M.; Machado, B.P. Simulação do carregamento de pelotas de minério de ferro em navios de porão conjugado com o método de elementos discretos. In Proceedings of the 37° Seminário de Logística–Proceedings, São Paulo, Brazil, 2–4 October 2018.
36. Chen, W.; Roberts, A.; Katterfeld, A.; Wheeler, C. Modelling the stability of iron ore bulk cargoes during marine transport. *Powder Technol.* **2018**, *326*, 255–264. [CrossRef]

37. Coetzee, C. Calibration of the discrete element method: Strategies for spherical and non-spherical particles. *Powder Technol.* **2020**, *364*, 851–878. [CrossRef]
38. Roessler, T.; Richter, C.; Katterfeld, A.; Will, F. Development of a standard calibration procedure for the DEM parameters of cohesionless bulk materials–part I: Solving the problem of ambiguous parameter combinations. *Powder Technol.* **2019**, *343*, 803–812. [CrossRef]
39. Weerasekara, N.S.; Powell, M.S.; Cleary, P.W.; Tavares, L.M.; Evertsson, M.; Morrison, R.D.; Quist, J.; Carvalho, R.M. Review The contribution of DEM to the science of comminution. *Powder Technol.* **2013**, *248*, 3–24. [CrossRef]
40. Grima, A.P.; Wypych, P.W. Investigation into calibration of discrete element model parameters for scale-up and validation of particle–structure interactions under impact conditions. *Powder Technol.* **2011**, *212*, 198–209. [CrossRef]
41. Hertz, H. Uber die Beruhrung fester elastischer Korper. *J. Fur Die Reine Und Angew. Math.* **1882**, *92*, 156–171. [CrossRef]
42. Mindlin, R.D.; Deresiewicz, H. Elastic Spheres in Contact Under Varying Oblique Forces. *J. Appl. Mech.* **1953**, *20*, 327–344. [CrossRef]
43. Carr, M.J.; Chen, W.; Williams, K.; Katterfeld, A. Comparative investigation on modelling wet and sticky material behaviours with a simplified JKR cohesion model and liquid bridging cohesion model in DEM. In Proceedings of the ICBMH 2016-12th International Conference on Bulk Materials Storage, Handling and Transportation, Proceedings, Darwin, Australia, 11–14 July 2016.
44. Ucgul, M.; Fielke, J.M.; Saunders, C. Three-dimensional discrete element modelling (DEM) of tillage: Accounting for soil cohesion and adhesion. *Biosyst. Eng.* **2015**, *129*, 298–306. [CrossRef]
45. Schulze, D. *Powders and Bulk Solids: Behavior, Characterization, Storage and Flow*; Springer: New York, NY, USA, 2007.
46. Johnson, K.L.; Kendall, K.; Roberts, A.D. Surface energy and the contact of elastic solids. *Proc. R. Soc. London. Ser. A Math. Phys. Sci.* **1971**, *324*, 301–313.
47. Ajmal, M.; Roessler, T.; Richter, C.; Katterfeld, A. Calibration of cohesive DEM parameters under rapid flow conditions and low consolidation stresses. *Powder Technol.* **2020**, *374*, 22–32. [CrossRef]
48. DCS Computing. LIGGGHTS(R) PUBLIC Documentation. Version 3.X (2016), CFDEM Research. Available online: https://www.cfdem.com/media/DEM/docu/Manual.html (accessed on 10 December 2024).
49. Huynh, T.Q.; Nguyen, T.T.; Indraratna, B. Evaluating cohesive models in discrete element simulation through drawdown test with new assessment perspectives. *Powder Technol.* **2024**, *452*, 120542. [CrossRef]
50. Easo, L.A.; Wassgren, C.R. Comparison of liquid bridge volume models in DEM simulations. In Proceedings of the AIChE Annual Meeting Proceedings (Vol. 1), San Francisco, CA, USA, 3–8 November 2013.
51. Govender, N.; Rajamani, R.; Wilke, D.N.; Wu, C.Y.; Khinast, J.; Glasser, B.J. Effect of particle shape in grinding mills using a GPU based DEM code. *Miner. Eng.* **2018**, *129*, 71–84. [CrossRef]
52. Coetzee, C.J. Calibration of the discrete element method and the effect of particle shape. *Powder Technol.* **2016**, *297*, 50–70. [CrossRef]
53. Zhou, H.; Hu, Z.; Chen, J.; Lv, X.; Xie, N. Calibration of DEM models for irregular particles based on experimental design method and bulk experiments. *Powder Technol.* **2018**, *332*, 210–223. [CrossRef]
54. Wensrich, C.M.; Katterfeld, A. Rolling Friction as a Technique for Modelling Particle Shape in DEM. *Powder Technol.* **2012**, *217*, 409–417. [CrossRef]
55. Ai, J.; Chen, J.F.; Rotter, J.M.; Ooi, J.Y. Assessment of Rolling Resistance Models in Discrete Element Simulations. *Powder Technol.* **2011**, *206*, 269–282. [CrossRef]
56. *56. ASTM A532*; Standard Specification for Abrasion-Resistant Cast Irons. ASTM, American Society for Testing and Materials: West Conshohocken, PA, USA, 2014.
57. ABNT, Associação Brasileira de Normas Técnicas. *NBR 17177: Transportadores Contínuos de Correia—Simulação do Escoamento de Granéis Sólidos em Chutes de Transferência Aplicando o Método dos Elementos Discretos (DEM)—Método para Calibração de Parâmetros de Contato—Padronização de Relatório de Simulação*; ABNT, Associação Brasileira de Normas Técnicas: Rio de Janeiro, Brasil, 2024.
58. Grima, A.; Wypych, P. Discrete Element Simulation of a Conveyor Impact-Plate Transfer: Calibration, Validation and Scale-Up. *Aust. Bulk Handl. Rev.* **2010**, *3*, 64–72.
59. Ilic, D. Bulk Solid Interactions in Belt Conveying Systems. Doctor of Philosophy of Mechanical. Ph.D. Thesis, The University of Newcastle, Callaghan, NSW, Australia, 2013; p. 304.
60. Mascarenhas, F.P.; Mesquita, A.L.A. Simulation of Transfer Chute Operation Using the Discrete Element Method. In Proceedings of the XXXIV Iberian Latin-American Congress on Computational Methods in Engineering (CILAMCE), Pirenópolis, Brazil, 10–13 November 2013.
61. Coetzee, C.J. Particle Upscaling: Calibration and Validation of the Discrete Element Method. *Powder Technol.* **2019**, *344*, 487–503. [CrossRef]
62. Li, C.; Honeyands, T.; O'dea, D.; Moreno-Atanasio, R. The Angle of Repose and Size Segregation of Iron Ore Granules: DEM Analysis and Experimental Investigation. *Powder Technol.* **2017**, *320*, 257–272. [CrossRef]

63. Tsuji, Y.; Tanaka, T.; Ishida, T. Lagrangian numerical simulation of plug flow of cohesionless particles in a horizontal pipe. *Powder Technol.* **1992**, *71*, 239–250. [CrossRef]
64. Mindlin, R.D. Compliance of Elastic Bodies in Contact. *J. Appl. Mech.* **1949**, *16*, 259–268. [CrossRef]
65. Sakaguchi, H.; Ozaki, E.; Igarashi, T. Plugging of the flow of granular materials during the discharge from a silo. *Int. J. Mod. Phys. B* **1993**, *7*, 1949–1963. [CrossRef]

**Disclaimer/Publisher's Note:** The statements, opinions and data contained in all publications are solely those of the individual author(s) and contributor(s) and not of MDPI and/or the editor(s). MDPI and/or the editor(s) disclaim responsibility for any injury to people or property resulting from any ideas, methods, instructions or products referred to in the content.